nature communications

Article

https://doi.org/10.1038/s41467-026-68545-7

Regulating Pb off-centering distortion for white-light emission in 2D halide perovskites

Received: 3 June 2025

Accepted: 9 January 2026

Published online: 21 January 2026

Check for updates

Yutong Zhang[1,2,8], Yuanyuan Guo[3,8], Minjun Feng[4,8], Shuyi Lin[5,8], Cheng Yang[1,6], Deyu Li[7], Yuexing Xia[1,2], Yiyang Gong[1,2], Xiaotian Bao[1], Yangguang Zhong[1], Zhiyong Zhang[1], Yubo Tian[1], Wenna Du[1,2], Shuai Yue[1,2], Bo Wu[6], Jun Xing[7] ✉, Jun Yin[5] ✉, Jianhui Fu[1,2] ✉ & Xinfeng Liu[1,2] ✉

Efficient tuning of structural distortion is an attractive approach for regulating self-trapped excitons emission properties of two-dimensional halide perovskites. Nevertheless, it remains elusive as to how the structural distortion is related with such emission. Here, we elucidate the relationship between structural distortion and the emission behavior of self-trapped excitons in two-dimensional lead bromide perovskites $(R\text{-}NH_3)_2PbBr_4$ (where R is the cyclic carbon group). We reveal that rather than the octahedral tilting distortion, the lone pair activity-induced Jahn-Teller distortion plays a significant role in self-trapped excitons emission. Consequently, with growing ring size of cyclic organic cation, the increased Jahn-Teller distortion results in a larger relative self-trapped excitons emission due to the enhanced short-range Holstein electron-phonon coupling strength. Our work clarifies the controversy of the structural distortion correlation on self-trapped excitons emission and provides valuable insights for structural engineering in white-light emitting applications of two-dimensional perovskites.

Owing to their unique properties—such as ease of fabrication, large absorption coefficients, and long-range balanced electron and hole diffusion lengths—three-dimensional (3D) halide perovskites have emerged as leading candidates for high-performance light-harvesting and light-emitting technologies[1–8]. Nevertheless, the practical implementation of these materials is constrained by their suboptimal moisture and thermal stability[9–12]. In contrast, their two-dimensional (2D) counterparts which inherit most of their excellent properties are more chemical stable owing to the hydrophobic features of large organic cation[13–16]. Meanwhile, 2D halide perovskites have also demonstrated their intriguing performance in light emitting devices (LEDs) and photodetectors[17–19]. 2D hybrid lead halide perovskites with a chemical formula of A_2PbX_4 (where A is the organic cation and X is the halide ion) are self-assembled quantum wells with one layer of inorganic PbX_6 octahedra sandwiched by bilayer of organic cation[20,21]. The inherent quantum and dielectric confinement within this bilayer configuration endows the material with a substantial exciton binding energy, making it an ideal candidate for high-efficiency light emission[22–25]. In particular, 2D lead bromide perovskites with broadband white-light emission and high photoluminescence quantum yield (PLQY) have recently garnered increasing attention for their potential applications in used as single-emitting material in white-light light-

[1]National Center for Nanoscience and Technology, Beijing, PR China. [2]University of Chinese Academy of Sciences, Beijing, PR China. [3]State Key Laboratory of Information Photonic and Optical Communications and School of Physical Science and Technology, Beijing University of Posts and Telecommunications (BUPT), Beijing, PR China. [4]Division of Physics and Applied Physics, School of Physical and Mathematical Sciences, Nanyang Technological University, Singapore, Singapore. [5]Department of Applied Physics, Hong Kong Polytechnic University, Kowloon, Hong Kong, PR China. [6]Guangdong Provincial Key Laboratory of Optical Information Materials and Technology & Institute of Electronic Paper Displays, South China Academy of Advanced Optoelectronics, South China Normal University, Guangzhou, PR China. [7]Key Laboratory of Eco-chemical Engineering, Ministry of Education, College of Chemistry and Molecular Engineering, Qingdao University of Science & Technology, Qingdao, PR China. [8]These authors contributed equally: Yutong Zhang, Yuanyuan Guo, Minjun Feng, Shuyi Lin. ✉e-mail: xingjun@qust.edu.cn; jun.yin@polyu.edu.hk; fujh@nanoctr.cn; liuxf@nanoctr.cn

emitting devices (w-LEDs) without requiring additional phosphors used in conventional w-LEDs, which usually results in lower PLQY and limited tunability of the color rendering index and temperature[26–28]. This is because of their broadband PL emission arising from recombination of self-trapped excitons (STEs) due to strong short-range Holstein electron-phonon coupling, which could simplify w-LEDs architectures by avoiding efficiency losses and spectral mismatches inherent to traditional multi-phosphor systems. However, the ionic nature of 2D halide perovskites and the weak noncovalent interactions between organic and inorganic components lead to a soft lattice and dynamic structural disorder, which complicates our understanding of the electron-phonon coupling and thereby STEs in these materials[29–33]. As a result, the manner in which structural distortions influence electron-phonon coupling strength and STE emission remains a subject of intense debate. To date, two primary distortion parameters have been identified as playing significant roles: out-of-plane inter-octahedral tilting and Jahn-Teller (JT)-like octahedral distortion. For instance, Smith et al. demonstrated that STE emission intensity correlates strongly with the degree of out-of-plane inter-octahedral tilting[34]. Such inter-octahedral distortion provides the necessary structural flexibility and distortion to form localized potential wells for exciton trapping. Nevertheless, Wang et al. hold that the JT-like octahedral distortion is mainly responsible for the intense STEs emission[35]. The JT distortion with asymmetric bond lengths is in fact the result of the Pb off-center displacement induced by the Pb $6s^2$ lone-pair activity[36,37]. Such lone-pair activity is due to the participation of partial lone-pair electrons in their hybridization with Br 4p orbitals within the $PbBr_6$ octahedra. On the other hand, the lone-pair activity will enhance the short-range Holstein exciton-phonon coupling by inducing strong local lattice distortions and structural instabilities, resulting in enhanced exciton-phonon coupling potential and promotes the self-trapping of excitons[36,38]. Furthermore, prior investigations have often centered on comparative analyses between halide perovskites possessing organic cations with markedly different molecular architectures (e.g., linear chains in contrast to aromatic moieties like benzene). Different types of organic cations may result in distinct Pb-X orbital interactions that alter the electronic states of the perovskites, which, in turn, would obfuscate our analysis of the extent to which organic cation-induced octahedral distortion affects the characteristics of STEs emission.

In this work, we elucidate the relationship between the organic cation-induced structural distortion and STEs emission in 2D lead bromide perovskites using temperature-dependent PL and ultrafast transient absorption (TA) spectroscopies complemented by density functional theory (DFT) calculations. We choose a representative 2D lead bromide perovskite $(R\text{-}NH_3)_2PbBr_4$, where R is the cyclic carbon group of C_nH_{2n-1} and n is the number of C atoms. The selected perovskites employ cyclic organic cations of the same structural class (cyclic alkylamines, C3-C6), which allows us to minimize the effect of varying organic cation type on the electronic structure of the perovskites. This in turn enables us to systematically study how distinct structural distortions are induced by a subtle difference of the organic cations (e.g., steric hindrance) and affect the electron-phonon coupling strength in 2D perovskites. We reveal that with increasing ring size of cyclic organic cation, the relative STEs emission's intensity as well as the phonon coherence intensity is enhanced significantly due to the enlarged electron-phonon coupling strength. Such enhanced STEs emission correlates strongly with the Pb off-center displacement-induced JT distortion instead of the octahedral tilting distortion. Meanwhile, temperature-dependent phonon coherence measurements reveal that larger ring size of cyclic organic cation increases the steric hindrance, resulting in a reduced lattice anharmonicity. Furthermore, DFT calculations show that the enhanced JT distortion results in an increase of exciton localization energy and Stokes shift. Our results provide fresh insights into the structural distortion correlation on the properties of STEs emission, which is not only of fundamental importance but also valuable for guiding the design and optimization of perovskite-based single-emitter w-LEDs.

Results

Characterization of two-dimensional perovskite

To investigate how the structural distortion affect the STEs emission, we first synthesized a series of 2D lead bromide perovskite single crystals (SCs) with different cyclic organic cations, cyclopropylamine (C3), cyclobutylamine (C4), cyclopentylamine (C5), and cyclohexylamine (C6) using the reported anti-solvent diffusion method[39,40]. Representative schematic of the crystal structure of C6 perovskite is shown in Fig. 1a. We then characterized these SCs and extracted their crystal structures using single-crystal XRD. Supplementary Tables 1 and 2 show the extracted crystal structures and the corresponding reliability factors of these SCs. As shown, the crystal structures are consistent with previous report[41]. Meanwhile, the reliability factors of our crystals are all smaller than 0.1, suggesting that our synthesized SCs are of high pure phase[42]. We obtained the SC flakes using the mechanical exfoliation method. We then characterized these SC flakes using scanning electron microscope (SEM) and energy-dispersive X-ray (EDX) spectroscopy. Supplementary Fig. 1 shows the SEM morphology and EDX images of these SC flakes. As shown, our prepared samples are flat in surface and the chemical elements are evenly distributed, which again suggests high quality of our synthesized samples. Moreover, we found that photoluminescence quantum yield (PLQY) of C3 and C5 perovskites are ~15%, much higher than those of C4 and C6 perovskite (~5%) (Supplementary Fig. 2). Although the PLQY varies from flake to flake (likely due to morphology differences), the consistency observed across the samples further verifies the high quality of our samples.

The optical properties of perovskites are in fact directly related to their structural distortions (Fig. 1b). Here, we consider two typical structural distortion parameters that have been widely acknowledged to correlate with STEs emission[34–36]: the out-of-plane component of the octahedral tilting distortion D_{out} (i.e., $180 - \theta_{out}$) and the Pb off-center displacement-induced JT distortion. Here, θ_{out} refers to the out-of-plane component of the angle between two adjacent $PbBr_6$ octahedra in the 2D perovskite inorganic layer. Details of the definition and calculation can be referred to Supplementary Fig. 3, Supplementary Table 3 and Supplementary Note 1. The Pb off-center displacement parameter σ_2^2 is calculated as $\sigma_2^2 = \frac{1}{2}\sum_{i=1}^{3}(\beta_i - 180)^2$, where β_i is the Br–Pb–Br bond angle between non-neighboring Pb–Br bonds. As shown in Fig. 1c, with increasing the $\text{-}NH_3^+$ penetration depth, the inorganic octahedral tilting distortion decreases associated with increase of Pb off-center displacement parameter. These structural changes can be understood based on the general rules of formation of a stable 2D perovskite structure[21]. In this scenario, as the ring size increases, which will increase the distance between the N and halogen atoms (both terminal and bridging, see Supplementary Fig. 4 and Supplementary Table 4 for their definitions and lengths, respectively). For example, when cyclic cation changes from C3 to C6, the penetration depth increases from 0.21 Å to 0.39 Å while the terminal distance L_1 increases from 3.36 Å to 3.39 Å. As a result, the hydrogen bonding between $\text{-}NH_3^+$ and axial Br becomes weaker, which in turn reduces the pulling force applied on the octahedra, leading to a decrease of the out-of-plane octahedral tilting distortion. Our argument is consistent with the literature report[43].

Cyclic organic cation-dependent emission

Next, we employ PL spectroscopy to investigate the properties of STEs emission. Figure 1d shows the PL spectrum of 2D lead bromide

https://doi.org/10.1038/s41467-026-68545-7

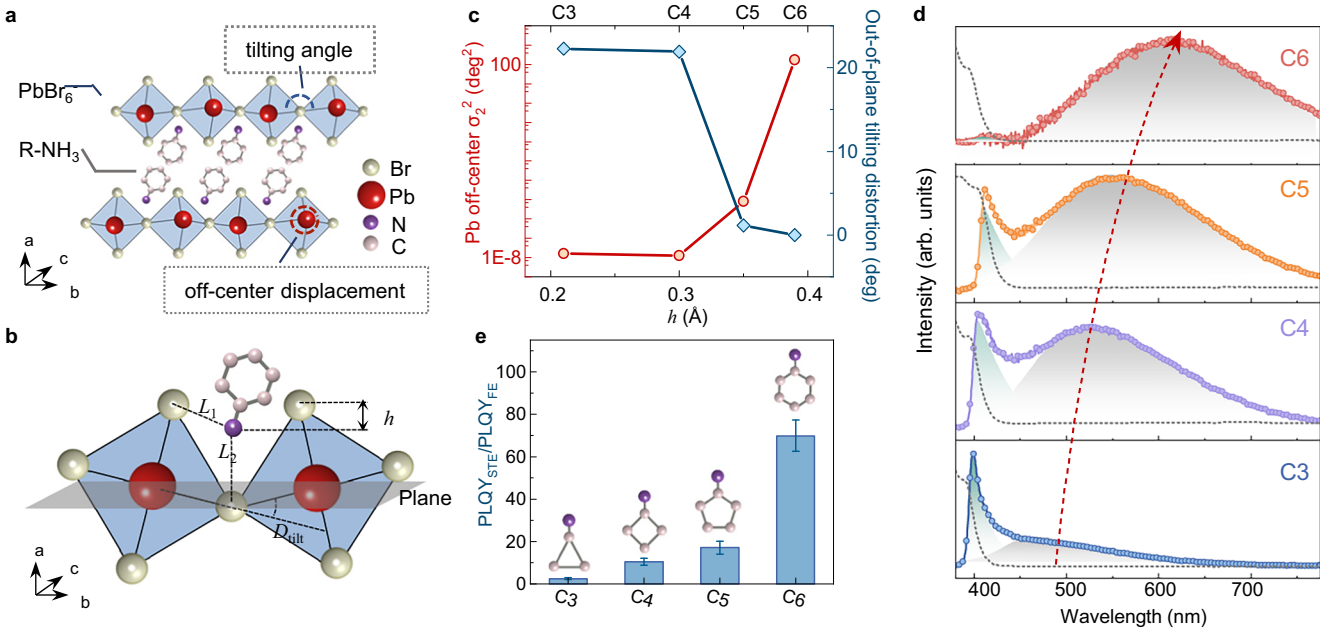

Fig. 1 | Cyclic organic cation-dependent STEs emission in 2D halide perovskites. **a** Schematic of a representative C6 perovskite. The crystal structure includes one layer of inorganic octahedra sandwiched by a bilayer of cyclic organic cation. The grey, red, purple, and pink balls represent the Br, Pb, N and C atoms, respectively. **b** Schematic of amnio group penetration and the corresponding terminal (L_1) and bridging (L_2) connections. h is the amnio group penetration depth. The graded plane refers to the out-of-plane of the octahedral layer and D_{tilt} corresponds to the titling distortion. **c** Extracted Pb off-center displacement parameter and the out-of-plane octahedral tilting distortion as a function of amnio group penetration depth. **d** PL (colored scatters) and absorption (black dotted curves) spectra of 2D halide perovskites with different cyclic organic cations. The cyan and black shaded areas refer to the curve-fits for FE and STE emission, respectively. The red-dashed curve with arrow is the guide for the eye, indicating the shifting of the STEs emission's center position. All the samples are excited with a CW laser at 360 nm. **e** The ratio of PLQY of STE emission to that of free exciton emission $PLQY_{STE}/PLQY_{FE}$ as a function of the ring size of cyclic cation. The error bar represents the standard deviation.

perovskites with different cyclic organic cations at room temperature. As shown, the shape of the PL spectrum strongly depends on the type of cyclic organic cations. The PL spectra of C3-C5 perovskites consist of a sharp peak from free exciton recombination and a below-bandgap broadband emission while that of C6 perovskite is dominated by the below-bandgap broadband emission[44]. Such below-bandgap broadband emission has been widely reported in 2D lead bromide perovskites such as (110) Pb-Br perovskites (N-MEDA)$PbBr_4$, (EDBE)$PbBr_4$ (N-MEDA = N^1-methylethane-1,2-diammonium and EDBE = 2,2′-(ethylenedioxy)bis(ethylammonium)) and $(C_6H_{11}NH_3)_2PbBr_4$, which can be attributed to the STEs recombination due to strong short-range Holstein electron-phonon interaction, leading to small polaron formation owing to exciton localization which is associated with large lattice distortions[34,45–47]. We note that this sub-bandgap broadband emission may arise from recombination of exciton localized at defects or impurities[48,49]. Such defect-induced recombination would lead to a saturated PL intensity when the pump intensity is relatively high[50]. Nevertheless, this is inconsistent with our power-dependent PL measurements which exhibit a linear dependence of the STEs emission intensity on the pump power (Supplementary Fig. 5). Thus, such below-bandgap broadband emission is due to the intrinsic STEs recombination owing to strong electron-phonon coupling. Other than the STEs recombination, the electron-phonon coupling also plays a significant role in the free exciton recombination, which leads to a reduced emission energy with increasing temperature (Supplementary Fig. 6). Meanwhile, with increasing ring size of cyclic organic cation, the out-of-plane octahedral tilting distortion is smaller and the Pb off-center displacement is larger (Fig. 1c) whereas the Stokes shift (Fig. 1d) and the ratio of PL intensity of STEs recombination to that of free exciton recombination $PLQY_{STE}/PLQY_{FE}$ (Fig. 1e) become larger, indicating a larger exciton localization energy and a stronger electron-phonon coupling. Note that though σ_2^2 of C3 and C4 perovskites are seemingly small, the lone-pair electrons are still present, which can be verified from their nonzero octahedral angle variance σ_1^2 and larger than unity bond length quadratic elongation $\langle\lambda\rangle$ (Table 1). On the other hand, there is no obvious correlation between the absolute PLQY of STEs emission and the ring size of cyclic cations (Supplementary Fig. 2 and Supplementary Table 5). The enhanced STEs emission with growing size of cyclic organic cation agrees well with recent reports in 3D lead perovskites, suggesting the STEs emission correlates more with the Pb off-center displacement-induced JT distortion[36]. In this scenario, the increasing ring size of cyclic cation enhances the 6 s^2 lone pair activity of the $PbBr_6$ octahedra, resulting in a stronger short-range Holstein interaction and an easier formation of small polarons. This can be understood as follows: as the ring size of cyclic cation increases, its steric hindrance will be larger, which will enhance the penetration of -NH_3^+ group into the $PbBr_6$ octahedral pockets. As a result, the eccentricity of the $PbBr_6$ octahedra is enhanced, which can be verified from Table 1. As shown, with growing ring size of cyclic cation, three out of four in-plane Pb-Br bond length are longer while one out of four in-plane Pb-Br bond length is shorter. Such aggravated eccentricity of the $PbBr_6$ octahedra will strengthen the mixture of $6s^2$ lone pair electrons with empty Pb and Br orbitals via the second-order JT effect, leading to an enhanced $6s^2$ lone pair activity of the $PbBr_6$ octahedra, thereby a stronger short-range Holstein interaction and easier formation of small polarons[37]. Moreover, our results are also consistent with the reports in $(PEA)_2PbBr_4$ (PEA= phenylethyl ammonium) and $(PMA)_2PbBr_4$, (PMA=phenylmethyl ammonium) with their PL spectra dominated by free exciton recombination and comparable to that of C3 perovskite, respectively[43]. Both exhibit relatively weak electron-phonon coupling strengths because of their negligible lone-pair activities (with $\sigma_1^2 \sim 0$, $\sigma_2^2 \sim 0.5$) and strong lattice rigidities due to the π-π stacking interactions between organic cations.

https://doi.org/10.1038/s41467-026-68545-7

Table 1 | Extracted structural distortion parameters of 2D lead bromide perovskites with different cyclic organic cations

	Pb off-center displacement parameter σ_2^2 (deg^2)	Octahedral angle variance σ_1^2 (deg^2)	Bond length quadratic elongation $\langle\lambda\rangle$	Out-plane tilting distortion D_{out} (deg)	In-plane tilting distortion D_{in} (deg)	Tilting distortion D_{tilt} (deg)
C3	1.6×10^{-8}	4.0329	1.0000012	22.27	31.17	33.82
C4	1.3×10^{-8}	8.74011	1.0000248	21.89	19.30	31.73
C5	8.0×10^{-6}	25.4142	1.0000873	1.14	26.30	26.54
C6	174.9	34.73785	1.0006711	0	21.14	21.13

The octahedral distortion parameters can be evaluated from the octahedral angle variance $\sigma_1^2 = \frac{1}{11}\sum_{i=1}^{12}(\alpha_i - 90)^2$, the Pb off-center displacement parameter $\sigma_2^2 = \frac{1}{2}\sum_{i=1}^{3}(\beta_i - 180)^2$, the bond length quadratic elongation $\langle\lambda\rangle = \frac{1}{6}\sum_{i=1}^{6}(d_i/d_0)^2$, where α_i, β_i, d_i and d_0 are the Br–Pb–Br bond angle, Br–Pb–Br bond angle between non-neighboring Pb–Br bonds, Pb–Br bond length, and mean Pb–Br bond length, respectively. For an ideal octahedron, $\sigma_1^2 = 0$, $\sigma_2^2 = 0$ and $\langle\lambda\rangle = 1$. Note that the σ_1^2 is not related with σ_2^2 given that $\sigma_2^2 \neq 0$ indicates local inversion symmetry breaking and thus long pair active. The out-plane tilting distortion is extracted from Br–Pb–Br bond angle and it is described in detail in Supplementary Note 1.

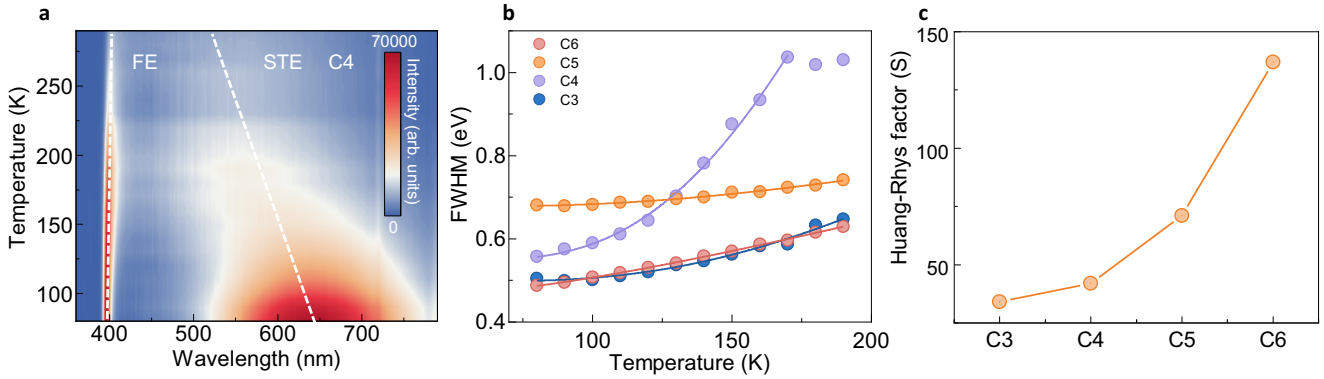

Fig. 2 | Cyclic organic cation-dependent electron-phonon coupling strength in 2D lead bromide perovskites. a Temperature-dependent PL spectrum of C4 perovskite excited with a CW laser at 360 nm. **b** Extracted FWHM of STEs emission for C3-C6 perovskites as a function of temperature. The solid lines are the curve-fits using Eq. (1). **c** The estimated Huang-Rhys factor S as a function of the ring size of cyclic cation.

Cyclic cation-dependent electron-phonon coupling strength

To verify the enhanced electron-phonon coupling strength, we conduct temperature-dependent PL measurements for all these SCs. Figure 2a shows a typical 2D contour-plot of temperature-dependent PL spectrum of C4 perovskite excited with a continuous wave (CW) laser at 360 nm. As shown, with increasing temperature, the center position of STEs emission blueshifts whereas that of free exciton emission remains nearly the same. Similar phenomenon is also observed in other three perovskites (Supplementary Fig. 5), which is likely because the energy level of STEs is higher due to the enhanced electron-phonon coupling strength at higher temperatures[51]. Notably, center positions of STEs emissions for C3 and C4 perovskites show significant blueshifts when the temperature increases from 78 K to 150 K. This is likely because of the involvement of additional scattering pathways from localized vibrational motion of organic cation. Meanwhile, owing to the presence of different scattering pathways such as from phonon and impurity scatterings, the PL linewidth of STEs emission will increase with temperature, which can be well described by the following equation[52]:

$$\mathrm{FWHM} = 2.36\sqrt{S}E_0 \cdot \sqrt{\coth\left(\frac{E_0}{2k_BT}\right)} \quad (1)$$

where FWHM is the full-width-at-half-maximum (FWHM) of STEs emission, E_0 is the phonon energy, S is the Huang-Rhys factor and k_B is the Boltzmann constant. By fitting the temperature-dependent PL linewidth using Eq. (1), we estimate the involved phonon energies that are in the range of 10-110 meV, in good agreement with previous reports[53–56]. Details of the curve-fittings are shown in Fig. 2b. The activated phonons are likely from optical phonons due to the torsional motion of the R-NH_3^+ group and the vibrational motion of Pb-Br network. These phonon energies in general can be also considered as the exciton-phonon renormalization energies[53,54]. Furthermore, they are dependent on the type of cyclic cation, suggesting that the organic cation plays a significant role in the vibrational properties of 2D halide perovskites. Figure 2c shows the estimated Huang-Rhys factor S for perovskites with different cyclic organic cations. As expected, S is larger than 20 for all these four perovskites, indicating a strong electron-phonon coupling and small polaron formation. In particular, the highest S of ~ 130 estimated for the C6 perovskite which to our knowledge is the largest value reported among 2D hybrid perovskites[51,57–59]. Moreover, it is larger for perovskites with larger cyclic organic cation, in good agreement with our previous results (Fig. 1d).

Cyclic organic cation-dependent coherent phonon dynamics

To further verify the enhanced electron-phonon coupling strength, we employed ultrafast TA spectroscopy to investigate the coherent phonon dynamics. Figure 3a shows the TA spectra of C6 perovskite pumped at 320 nm at 80 K. The TA spectrum features a broad photo-induced absorption (PIA) band between 400 to 600 nm (Supplementary Fig. 7). Such broad below-bandgap PIA which has been widely reported in other perovskites can be attributed to the transition of STEs to high-energy states[60,61]. Meanwhile, strong oscillations are superimposed on the TA kinetics. The presence of these oscillations in general signifies the presence of coherent phonons which are launched by resonant-impulsive stimulated Raman scattering[62–64]. In this case, a femtosecond laser pulse generates coherent phonon wavepackets and induces periodic lattice displacement. Such lattice displacement then modulates the complex refractive index, which in turn modifies transmittance of the sample. We extracted the oscillatory components from the TA kinetics by subtracting the carrier population contributions which are fitted using a sum of multiple-exponential decay functions. Representative TA kinetics and the curve-fit are

https://doi.org/10.1038/s41467-026-68545-7

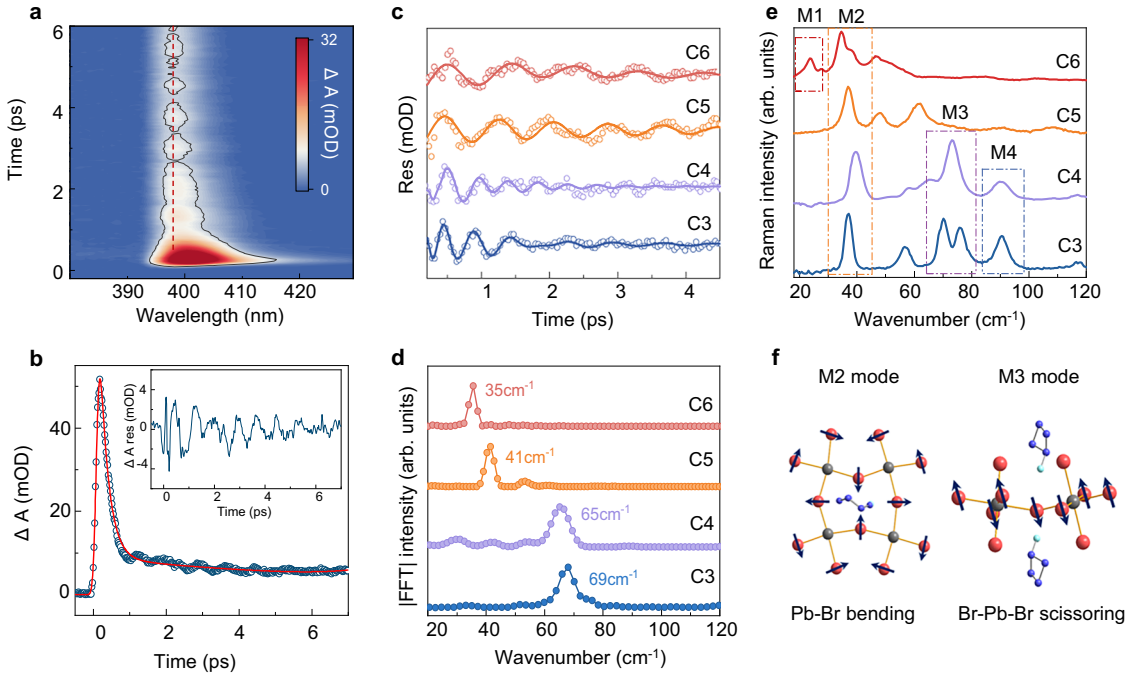

Fig. 3 | Cyclic organic cation-dependent coherent phonon dynamics in 2D lead bromide perovskites. a 2D contour-plot of TA spectrum of C6 perovskite pumped at 320 nm at 80 K. **b** TA kinetics and the curve-fits probed at 398 nm. The inset is the residual of the fitting. **c** TA oscillation kinetics and the curve-fits probed at 398 nm for C3-C6 perovskites. **d** FFT spectrum of the oscillation kinetics for C3-C6 perovskites. **e** Steady-state Raman spectra of C4-C6 perovskites at 80 K. The samples were excited by a CW laser at 633 nm. The colored rectangles refer to the different phonon modes activated in TA measurements. **f** Schematic of M2 and M3 phonon modes of $PbBr_6$ octahedra motions. The M2 and M3 modes correspond to Pb-Br bending and Br-Pb-Br scissoring motions, respectively.

shown in Fig. 3b. Figure 3c shows the cyclic organic cation-dependent oscillation kinetics. It is obvious that the oscillation period increases when the ring size of cyclic organic cation is larger. We then conduct Fourier transforming of these oscillation kinetics to extract the activated coherent phonon modes. As shown in Fig. 3d, the activated phonon modes are in the range of 30–70 cm^{-1}. Meanwhile, only one phonon mode is present for all the perovskites, and the launched phonon energy is smaller for perovskite with larger cyclic organic cation.

To explore the properties of these activated phonon modes, we perform non-resonant steady-state Raman scattering measurements for all the perovskites at 80 K. Consistently, the launched coherent phonon modes match well with the Raman measurements. At 80 K, four phonon modes below 100 cm^{-1} labeled as M1, M2, M3 and M4 are present in the Raman spectrum (Fig. 3e and Supplementary Table 6). These phonon modes can be assigned to vibrational motion of the $PbBr_6$ octahedra and are different from other high-frequency modes above ~100 cm^{-1} that are dominated by localized motion of organic cations[53,62]. In particular, M2 mode in the range of 30 to 45 cm^{-1} refers to the in-plane octahedral rocking motion, whereas M3 mode in the range of 65 to 80 cm^{-1} corresponds to the out-of-plane shear motion of the Pb-Br network. Details of these two modes can be found in Fig. 3f and Supplementary Fig. 8. Furthermore, compared with the steady-state Raman measurements, the activated coherent phonon modes for C3 and C4 perovskites correspond to the M3 mode, whereas for C5 and C6 perovskites, they refer to the M2 mode (Fig. 3d)[41]. On the other hand, for C3-C5 perovskites, the neighboring octahedral layer stacking corresponds to an eclipsed conformation, whereas for C6 perovskite, it refers to the staggered conformation (Supplementary Fig. 9). This indicates that the activated phonon modes are not likely to correlate with the octahedral layer conformation. Here, we hypothesize that the activated phonon modes instead may be relevant with the structural distortions of the perovskites. For C3 and C4 perovskites with larger out-of-plane octahedral tilting distortions owing to the shallower amnio group penetrations because of their smaller ring-sized cyclic cations, under femtosecond laser pulse excitation, the octahedral network is probably to undergo the out-of-plane shear motions (i.e., M3 mode). In contrast, for C5 and C6 perovskites with much smaller out-of-plane octahedral tilting distortions because of enhanced steric hindrance from larger ring-sized cyclic cations, the out-of-plane octahedral motions are likely to be restricted, and the octahedral network is more likely to undergo the in-plane rocking motions (i.e., M2 mode). A clear understanding of the correlation between the structural distortions and the activated coherent phonon modes is, however, beyond the scope of our work. Future work is needed to clarify such correlation. It is worth noting that the activated coherent phonon modes in the phonon coherence measurements correspond to the excited-state vibrational packets and thus are likely different from the ground-state modes probed in the steady-state Raman measurement[54]. Meanwhile, only modes with their periods larger than the pump pulse duration can be activated in ultrafast TA measurements[65]. This suggests that other high-energy modes though not activated in our pump-probe measurements, may still couple strongly with the excitons.

Notably, in contrast to conventional phonon coherence measurements based on ultrafast TA spectroscopy, where oscillations typically appear on both the blue and red sides of the photobleaching band, the phonon-induced oscillation in this study occurs within the photoinduced absorption (PIA) region. This suggests that the activated coherent phonons are likely involved in the STEs' formation process. Similar phenomenon has also been reported in other semiconductors such as $Cs_2AgBiBr_6$ and colloidal CdSe nanoplatelet superlattices[60,61]. To further corroborate such phonon-assisted STEs formation process, we compare the phonon-induced PIA oscillation amplitude for these perovskites with different cyclic organic cations. As expected, when the ring size of cyclic organic cation is larger, the phonon-induced FFT intensity increases (Supplementary Fig. 10), indicating a stronger electron-phonon coupling strength. This again is in good agreement with our previous results (Fig. 2c).

https://doi.org/10.1038/s41467-026-68545-7

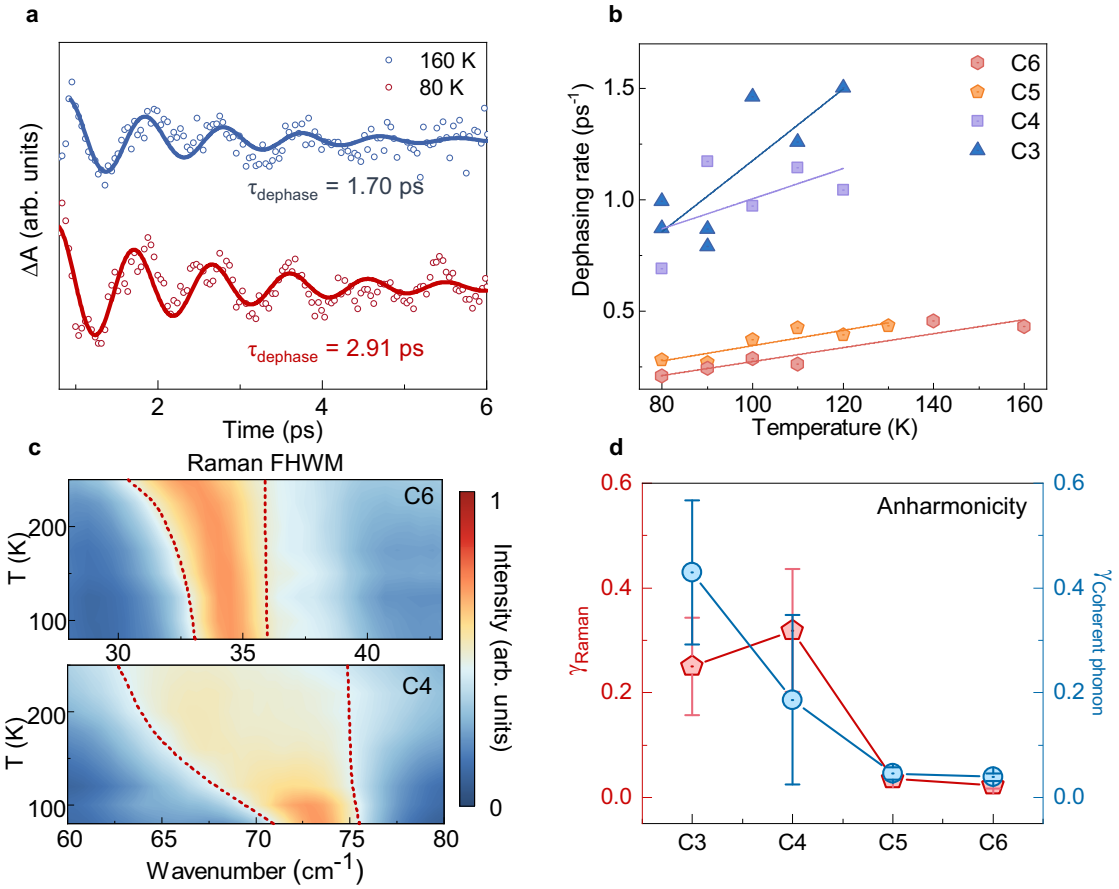

Fig. 4 | Cyclic organic cation-dependent lattice anharmonicity in 2D lead bromide perovskites. a TA oscillation kinetics and the curve-fits probed at 398 nm for C6 perovskite at 80 K and 160 K. **b** Estimated temperature-dependent dephasing rates of 2D perovskites for different cyclic organic cations. **c** Temperature-dependent Raman spectrum for C6 (top panel) and C4 (bottom panel) perovskites. The red dashed lines correspond to the FWHM of the Raman peak. The spectra were collected using a CW laser at 633 nm. **d** Estimated anharmonic coefficients from Raman (red line with scatter) and TA (blue line with scatter) measurements as a function of the ring size of cyclic cation. The error bars are from the curve-fits in (**b**) and Supplementary Fig. 14b.

Cyclic organic cation-dependent lattice anharmonicity

Earlier reports claim that when the perovskite lattice is softer, the electron-phonon coupling strength will be larger, which will increase the probability of carrier localization, resulting in a stronger STEs emission[66,67]. This is because the soft lattices with weaker interatomic forces allow for larger amplitude atomic vibrations for a given energy. These larger displacements will lead to a greater modulation of the electronic potential experienced by the carriers, enhancing the scattering probability and thereby the coupling strength. However, this needs not be the case for hybrid perovskites. This is because electron-phonon coupling strength is fundamentally governed by the complex interplay between the material's electronic structure and the anharmonicity of the specific phonon modes involved in the interaction[62,63,68,69]. While the organic cation plays only a secondary or auxiliary role, the latter is expected to exert a more significant influence on the electron-phonon coupling strength as the electronic states are primarily dominated by the valence states of the inorganic octahedra[65,70]; earlier work suggests that the organic cations contribute more significantly to the overall lattice rigidity[66]. Hence, it is highly likely that the electron-phonon coupling strength contributed by the inorganic octahedra is high, while the anharmonicity from the organic cation is small.

To verify our hypothesis, we investigate the temperature-dependent coherent phonon dynamics of these 2D lead bromide perovskites. Figure 4a displays representative coherent phonon dynamics of C6 perovskite measured at 80 and 160 K. As shown, compared to the dynamics at 80 K, the coherent phonon dephases much faster at 160 K. Considering high quality of our samples, the decrease of phonon dephasing time with temperature is likely because of enhanced phonon-phonon scattering at higher temperatures[57,71]. To provide insights into the lattice anharmonicity, we fit the phonon-induced TA oscillation kinetics using a damped sine function, $y = Ae^{-\frac{t}{\tau}}\sin(\omega t + \phi)$, where A, τ, ω, and ϕ are the amplitude, dephasing time, phonon frequency and initial phase, respectively. From fitting of the oscillation kinetics, we estimate the phonon dephasing time of ~ 2.9 and ~ 1.7 ps for temperatures at 80 and 160 K, respectively. Similarly, shorter phonon dephasing time at higher temperatures is also observed among other three perovskites (Supplementary Fig. 11 and Supplementary Table 7). Meanwhile, negligible phonon shift is present for all the four perovskites, indicating the absence of phase transition across the temperature range of interest (Supplementary Fig. 12).

Figure 4b shows the temperature-dependent phonon dephasing rate (i.e., $\Gamma = 1/\tau$) as a function of temperature for all the four perovskites. As mentioned above, the phonon dephasing rate increases with temperature because of enhanced phonon-phonon scattering at high temperatures. Compared to C5 and C6 perovskites, phonon dephasing rates of C3 and C4 perovskites are much higher, suggesting a much larger phonon-phonon scattering rate. Consistently, the Raman linewidths of C3 and C4 perovskites are much larger, as shown in Fig. 4c. The larger phonon dephasing rates of C3 and C4 perovskites are possibly because of the much easier reorientation of their smaller organic cations, which would likely induce dynamic disorders and thereby an increased phonon scattering rate[27,36,66]. Similar phenomenon has been reported in conventional semiconductors such as

group-IV metal chalcogenides and 3D halide perovskites[72–74]. Meanwhile, such cyclic organic cation dependence also indicates that the organic cation plays a significant role in the dephasing rate of the activated phonons of the inorganic octahedra, in good agreement with previous reports[57,63]. The phonon-phonon scattering-induced dephasing rate can be in general described using the equation[68,75]:

$$\Gamma = \Gamma_0 + \gamma_0 \left[1 + \frac{2}{\exp\left(\frac{\hbar\omega}{2k_B T}\right) - 1} \right] \quad (2)$$

where γ_0 is the anharmonic coefficient, $\hbar\omega$ is the phonon energy, and Γ_0 is the temperature-independent phonon dephasing rate which is generally dominated by the defect scattering[68]. Details of the curve-fits using Eq. (3) are shown in Fig. 4b and Fig. 4d. As shown, the dephasing rates of C5 and C6 perovskites increase much slower with temperature compared to those of C3 and C4 perovskites, suggesting the lattice of the former two are more rigid. This is likely because of the steric hindrance effect from large cyclic organic cations that limits vibrational motions of the inorganic octahedra. To further verify such steric hindrance effect from cyclic organic cations, we investigate the temperature dependence of the incoherent phonon lifetime from steady-state Raman measurements (Supplementary Fig. 13). We fit the Raman peak using the Lorentz equation $y = \frac{A}{\pi} \frac{\Gamma_R}{(\omega-\omega_i)^2 + {\Gamma_R}^2}$, where A is the integrated intensity of the peak, Γ_R is the Raman linewidth which is usually dominated by the phonon-phonon interaction, and ω_i is the phonon frequency[76]. Temperature-dependent phonon decay rates $\gamma_R = \pi c \Gamma_R$ (where c is the speed of light in the vacuum) and the curve-fits using Eq. (2) of the associated phonon modes for C3-C6 perovskites are displayed in Supplementary Fig. 14 and Fig. 4d. Consistently, γ_R of C3 and C4 perovskites exhibit much more obvious temperature dependences compared to C5 and C6 perovskites (Supplementary Table 8). The reduced lattice stiffness of 2D perovskites with increasing ring size of cyclic cation can be further validated from the strain-dependent Raman measurements (Supplementary Fig. 15, Supplementary Fig. 16 and Supplementary Table 9). Therefore, both our phonon coherence and Raman measurements demonstrate a weaker lattice anharmonicity in halide perovskites that show stronger electron-phonon coupling strength, indicating that the lattice softness needs not to play a significant role in the strong electron-phonon coupling.

Discussion

Our PL and TA measurements, modulated by different cyclic organic cations, reveal that the JT distortion induced by Pb off-center displacement is closely correlated with the STEs emission. The enhanced STEs emission with increasing ring size of cyclic cation is attributed to the increased JT distortion, leading to a stronger electron-phonon coupling. To unravel the mechanism behind JT distortion-induced STEs emission, we conducted DFT calculations. The optimized crystal structures, band structures and projected density of states (p-DOS) are shown in Supplementary Fig. 17. Figure 5a and b show the partial charge densities of the electron and hole in the STE state for C3 and C6 perovskites. In the pristine 2D hybrid perovskites, both electron and hole wavefunctions are delocalized across the lattice (Supplementary Fig. 17). Upon introducing JT distortion, both electron and hole become localized, confirming the formation of STEs[35].

Furthermore, we calculated the configuration coordinate diagrams for all four perovskites and extracted the lattice deformation energy (E_d, the change in ground-state energy resulting from STE formation) and the exciton self-trapping energy (E_{st}, the energy difference between the free exciton and the STE). As shown in Fig. 5c and Supplementary Fig. 18, STEs formation is accompanied by lattice distortions, in good agreement with the polaron formation process. Importantly, as the ring size of cyclic cation increases, the exciton self-trapping energy also increases, leading to a reduction in the emission energy (Fig. 5d), consistent with our PL results (Fig. 1d). The increased E_{st} would reduce the probability of exciton delocalization via thermal phonon and defect scatterings, thereby enhancing STEs emission. This indicates that the critical role of JT distortion in modulating the exciton self-trapping energy.

Apart from demonstrating the structural distortion correlation with STEs emission, we also show that with increasing ring size of cyclic cation, the perovskite's lattice is much more rigid while it exhibits a much stronger electron-phonon coupling strength, which stands contrasts with the typical behavior of STEs[77]. This indicates that while the steric hindrance from large organic cations plays a non-trivial role in reducing the phonon anharmonicity and lattice softness, it has more impact on the structural distortion induced by Pb off-center displacement. As a result, the resultant JT distortion is larger, leading to a stronger STEs emission.

In summary, through cyclic cation-dependent optical measurements, we correlate directly the structural distortion with STEs emission in 2D lead bromide perovskites. The increasing ring size of cyclic cation leads to an enhanced steric hindrance that amplifies the Pb off-centering displacement and lone pair activity, resulting in a stronger short-range Holstein electron-phonon interaction and thereby an enhanced STEs emission. Importantly, we show that lattice softness is not a prerequisite for strong electron-phonon coupling strength in 2D lead bromide perovskites. Our findings lay the foundation for the fundamental understanding of the structural distortion-property relationship in 2D lead bromide perovskites which will open new pathways for the materials design and optimization by leveraging their distortion degree of freedom.

Methods

Sample preparation

The $(R\text{-}NH_3)_2PbBr_4$ single crystal micro-platelets were synthesized using the anti-solvent method. 0.5 mmol alkylammonium bromide and 0.25 mmol $PbBr_2$ were dissolved in a mixed solvent of 0.25 mL DMF and 0.25 mL DMSO in a 5 mL vial. The small vial was put in a big vial with 10 mL chloroform and kept at 40 °C. After several days, the perovskite crystals were formed in the small vial. The ORTEP-style illustrations of 2D perovskites with different cyclic cations are shown in Supplementary Fig. 19. The X-ray crystallographic coordinates for structures reported in this study have been deposited at the Cambridge Crystallographic Data Centre (2518067-2518070).

Sample characterization

Single-crystal XRD were performed on Bruker D8 Venture under 150 K. Energy-dispersive X-ray spectroscopy (EDX) mapping was conducted on an FEI TITAN CUBED THEMIS G2300 equipped with a spherical aberration corrector.

Transient absorption measurements

Micro-TA measurements were performed on perovskite microplatelets using a home-built microscopic system integrated with a HELIOS platform. A frequency-tunable pump beam was generated by pumping an optical parametric amplifier (Coherent, OperA Solo) with the fundamental 800 nm output (1 kHz, 100 fs) of a Coherent Astrella regenerative amplifier The white light continuum probe beam from 320 to 775 nm (1.6 to 3.9 eV) was obtained by focusing a small portion of the fundamental 800 nm beam on a sapphire crystal.

Photoluminescence measurements

Photoluminescence (PL) spectra were recorded with a Princeton Instruments SP2500i spectrometer system. Excitation was focused through a 100× Leica objective (NA = 0.95), and the backscattered emission was collected by the same lens. The signal was then fiber-coupled to the spectrometer and detected by a liquid nitrogen-cooled CCD.

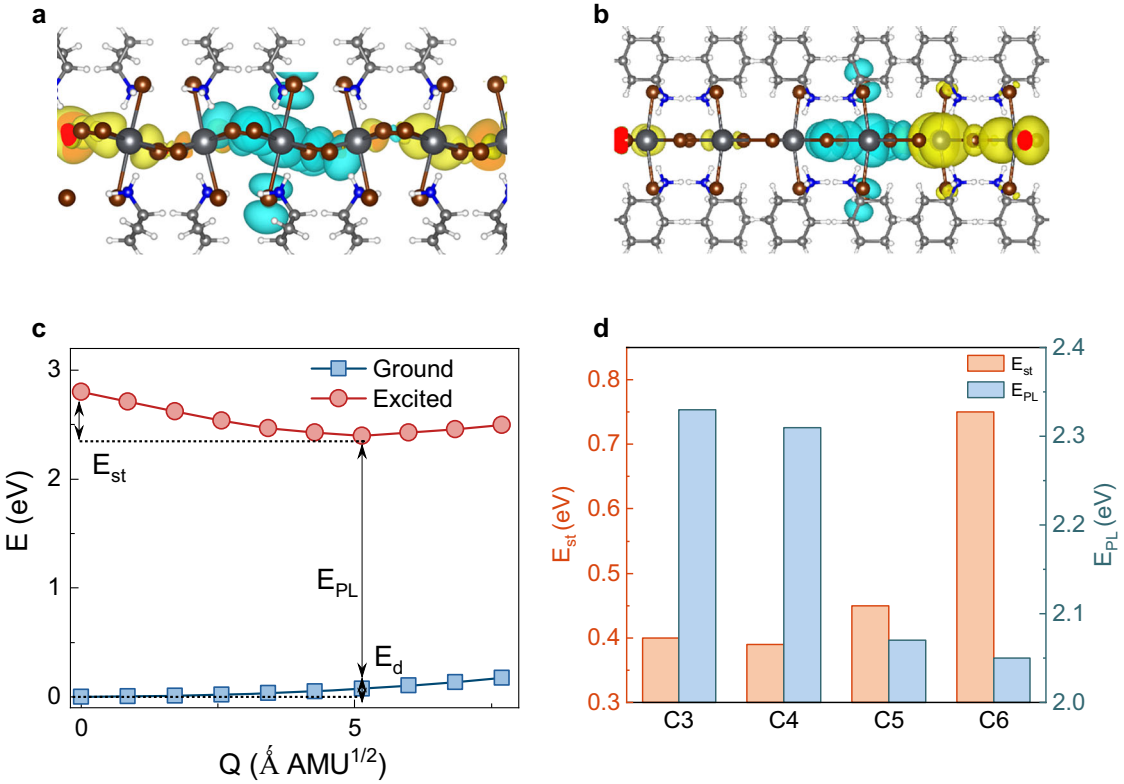

Fig. 5 | Structural distortion correlation with strong STEs emission in 2D lead bromide perovskites revealed by DFT calculations. Calculated partial charge densities of electron (cyan) and hole (yellow) wavefunctions in the STE state for C3 (**a**) and C6 (**b**) perovskites. **c** Representative calculated configuration coordinate diagram of the ground and excited states for C3 perovskite. E_{st}, E_{PL}, and E_d are the energies of self-trapping, emission, and lattice deformation, respectively. **d** Calculated E_{st} and E_{PL} for C3-C6 perovskites.

Density functional theory calculations

The density functional theory (DFT) calculations were performed using the Vienna Ab initio Simulation Package (VASP), employing the Perdew-Burke-Ernzerhof (PBE) functional within the generalized gradient approximation (GGA) for the exchange-correlation energy. Crystal structure relaxations and electronic structure calculations for the 2D hybrid perovskites (C3, C4, C5, and C6) were carried out using a plane-wave cutoff of 550 eV and a 2 × 3 × 3 Monkhorst-Pack *k*-mesh grid. The convergence criteria for total energy and forces were set to 10^{-5} eV and 0.01 eVÅ^{-1}, respectively. The time-dependent DFT simulations were carried out with CP2K to probe the excited states of 2D hybrid perovskites. Calculations employed a 3 × 3 × 1 supercell of C3-C6 at the *Γ*-point in both ground and excited states. The setup used molecularly optimized double-zeta valence polarization basis sets, PBE exchange-correlation functional, and Goedecker-Teter-Hutter pseudopotentials with a 400 Ry cutoff. To model the structural response upon photo-excitation, octahedral Jahn-Teller distortions were introduced by shortening four Pb-Br bonds and elongating two Pb-Br bonds within each octahedron, facilitating the formation of self-trapped excitonic states. To construct a one-dimensional configuration coordinate diagram, atomic positions were linearly interpolated between the excited-state $R^e_{k.i}$ and ground-state $R^g_{k.i}$ equilibrium geometries. The overall displacement was defined as $\Delta Q = \sqrt{\sum_{k.i} M_k (R^e_{k.i} - R^g_{k,i})^2}$, where M is the atomic mass, $i = (x, y, z)$, k labels each atom and R is the atomic coordinate, respectively. The coordinate Q was varied from 0 to ΔQ to trace the potential energy surface along the structural distortion path.

Data availability

All data supporting the findings of this study are available within the paper and its Supplementary files. Crystallographic data for the structures reported in this Article have been deposited at the Cambridge Crystallographic Data Centre, under deposition numbers (2518067-2518070). Copies of the data can be obtained free of charge via https://www.ccdc.cam.ac.uk/structures/. Any additional information related to the study is available from the corresponding author upon request.

Code availability

Vienna Ab initio Simulation Package (VASP), used for band structure and DOS calculations, is available at https://www.vasp.at/. CP2K used for STE calculations is available at https://www.cp2k.org/.

References

1. Wu, X. et al. Exciton polariton condensation from bound states in the continuum at room temperature. *Nat. Commun.* **15**, 3345 (2024).
2. Song, J. et al. Continuous-wave pumped perovskite lasers with device area below 1 μm2. *Adv. Mater.* **35**, 2302170 (2023).
3. Zhang, S. et al. All-optical control of rotational exciton polaritons condensate in perovskite microcavities. *ACS Photonics* **10**, 2414–2422 (2023).
4. Du, W. et al. All optical switching through anistropic gain of CsPbBr3 single crystal microplatelet. *Nano Lett.* **22**, 4049–4057 (2022).
5. Wang, Y. et al. Octahedral units in halide perovskites. *Nat. Rev. Chem.* (2025).
6. Xing, G. et al. Transcending the slow bimolecular recombination in lead-halide perovskites for electroluminescence. *Nat. Commun.* **8**, 14558 (2017).
7. Zhang, Y. et al. Ferroelectricity in a semiconducting all-inorganic halide perovskite. *Sci. Adv.* **8**, eabj5881 (2022).

8. Lee, K. J. et al. Gigantic suppression of recombination rate in 3D lead-halide perovskites for enhanced photodetector performance. *Nat. Photonics* **17**, 236–243 (2023).
9. Metcalf, I. et al. Synergy of 3D and 2D Perovskites for durable, efficient solar cells and beyond. *Chem. Rev.* **123**, 9565–9652 (2023).
10. Yu, D., Cao, F., Su, C. & Xing, G. Exploring, identifying, and removing the efficiency-limiting factor of mixed-dimensional 2d/3D perovskite solar cells. *Acc. Chem. Res.* **56**, 959–970 (2023).
11. Ajayakumar, A., Muthu, C., V. Dev, A., Pious, J. K. & Vijayakumar, C. Two-dimensional halide perovskites: approaches to improve optoelectronic properties. *Chem. Asian J.* **17**, e202101075 (2022).
12. Li, S. et al. High-efficiency and thermally stable FACsPbI3 perovskite photovoltaics. *Nature* **635**, 82–88 (2024).
13. Zhang, S. et al. Moiré superlattices in twisted two-dimensional halide perovskites. *Nat. Mater.* **23**, 1222–1229 (2024).
14. Peng, S. et al. Regulation of quantum Wells width distribution in 2D perovskite films for photovoltaic application. *Adv. Funct. Mater.* **32**, 2205289 (2022).
15. Yan, L. et al. Charge-carrier transport in quasi-2D Ruddlesden–Popper perovskite solar cells. *Adv. Mater.* **34**, 2106822 (2022).
16. Jiang, Y. et al. Reducing the impact of Auger recombination in quasi-2D perovskite light-emitting diodes. *Nat. Commun.* **12**, 336 (2021).
17. Jiang, N. et al. Manipulating phase and defect distribution of Quasi-2D perovskites via a synergistic strategy for enhancing the performance of blue light-emitting diodes. *ACS Appl. Mater. Interfaces* **17**, 8024–8035 (2025).
18. Yue, Y. et al. Ultrafast photoexcitation induced passivation for Quasi-2D perovskite photodetectors. *Adv. Mater.* **36**, 2407347 (2024).
19. Lee, Y. H. et al. Large-scale 2D perovskite nanocrystals photodetector array via ultrasonic spray synthesis. *Adv. Mater.s* **n/a**, 2417761.
20. Zhu, C. et al. Supramolecular assembly of blue and green halide perovskites with near-unity photoluminescence. *Science* **383**, 86–93 (2024).
21. Li, X., Hoffman, J. M. & Kanatzidis, M. G. The 2D halide perovskite rulebook: how the spacer influences everything from the structure to optoelectronic device efficiency. *Chem. Rev.* **121**, 2230–2291 (2021).
22. Chen, X. et al. Tuning spin-polarized lifetime in two-dimensional metal–halide perovskite through exciton binding energy. *J. Am. Chem. Soc.* **143**, 19438–19445 (2021).
23. Sun, Q. et al. Ultrafast and high-yield polaronic exciton dissociation in two-dimensional perovskites. *J. Am. Chem. Soc.* **143**, 19128–19136 (2021).
24. Qin, T. et al. Coherent exciton spin relaxation dynamics and exciton polaron character in layered two-dimensional lead-halide perovskites. *ACS Nano* **19**, 4186–4194 (2025).
25. Zhou, H. et al. Robust excitonic light emission in 2D tin halide perovskites by weak excited state polaronic effect. *Nat. Commun.* **15**, 8541 (2024).
26. Cheng, X. et al. Two novel two-dimensional organic–inorganic hybrid lead halides with broadband emission for white-light-emitting diodes. *ACS Appl. Mater. Interfaces* **15**, 32506–32514 (2023).
27. Han, X.-B., Jing, C.-Q., Zu, H.-Y. & Zhang, W. Structural descriptors to correlate Pb ion displacement and broadband emission in 2D halide perovskites. *J. Am. Chem. Soc.* **144**, 18595–18606 (2022).
28. Han, Y. et al. Exciton self-trapping for white emission in 100-oriented two-dimensional perovskites via halogen substitution. *ACS Energy Lett.* **7**, 453–460 (2022).
29. Yamada, Y. & Kanemitsu, Y. Electron-phonon interactions in halide perovskites. *NPG Asia Mater.* **14**, 48 (2022).
30. Fu, J. et al. Organic and inorganic sublattice coupling in two-dimensional lead halide perovskites. *Nat. Commun.* **15**, 4562 (2024).
31. Mayers, M. Z., Tan, L. Z., Egger, D. A., Rappe, A. M. & Reichman, D. R. How lattice and charge fluctuations control carrier dynamics in halide perovskites. *Nano Lett.* **18**, 8041–8046 (2018).
32. Mozur, E. M. & Neilson, J. R. Cation dynamics in hybrid halide perovskites. *Annu. Rev. Mater. Res.* **51**, 269–291 (2021).
33. Biswas, S. et al. Exciton polaron formation and hot-carrier relaxation in rigid Dion–Jacobson-type two-dimensional perovskites. *Nat. Mater.* **23**, 937–943 (2024).
34. Smith, M. D., Jaffe, A., Dohner, E. R., Lindenberg, A. M. & Karunadasa, H. I. Structural origins of broadband emission from layered Pb–Br hybrid perovskites. *Chem. Sci.* **8**, 4497–4504 (2017).
35. Wang, X. et al. Atomistic mechanism of broadband emission in metal halide perovskites. *J. Phys. Chem. Lett.* **10**, 501–506 (2019).
36. Huang, X. et al. Understanding electron–phonon interactions in 3D lead halide perovskites from the stereochemical expression of 6s2 lone pairs. *J. Am. Chem. Soc.* **144**, 12247–12260 (2022).
37. Fu, Y., Jin, S. & Zhu, X. Y. Stereochemical expression of ns2 electron pairs in metal halide perovskites. *Nat. Rev. Chem.* **5**, 838–852 (2021).
38. Gu, J. et al. Correlating photophysical properties with stereochemical expression of 6s2 lone pairs in two-dimensional lead halide perovskites. *Angew. Chem. Int. Ed.* **62**, e202304515 (2023).
39. Zhang, M. et al. Molecular engineering towards efficientwhite-light-emitting perovskite. *Nat. Commun.* **12**, 4890 (2021).
40. Niu, L. et al. Predictably synthesizing a library of white-light-emitting perovskites. *Sci. China Chem.* **66**, 760–767 (2023).
41. Billing, D. G. & Lemmerer, A. Inorganic–organic hybrid materials incorporating primary cyclic ammonium cations: The lead bromide and chloride series. *CrystEngComm* **11**, 1549–1562 (2009).
42. Groom, C. R., Bruno, I. J., Lightfoot, M. P. & Ward, S. C. The Cambridge Structural Database. *Acta Crystallogr. Sect. B* **72**, 171–179 (2016).
43. Du, K. -z et al. Two-dimensional lead(II) halide-based hybrid perovskites templated by acene alkylamines: crystal structures, optical properties, and piezoelectricity. *Inorg. Chem.* **56**, 9291–9302 (2017).
44. Tao, W., Zhang, C., Zhou, Q., Zhao, Y. & Zhu, H. Momentarily trapped exciton polaron in two-dimensional lead halide perovskites. *Nat. Commun.* **12**, 1400 (2021).
45. Dohner, E. R., Jaffe, A., Bradshaw, L. R. & Karunadasa, H. I. Intrinsic white-light emission from layered hybrid perovskites. *J. Am. Chem. Soc.* **136**, 13154–13157 (2014).
46. Dohner, E. R., Hoke, E. T. & Karunadasa, H. I. Self-assembly of broadband white-light emitters. *J. Am. Chem. Soc.* **136**, 1718–1721 (2014).
47. Yangui, A. et al. Optical investigation of broadband white-light emission in self-assembled organic–inorganic perovskite (C6H11NH3)2PbBr4. *J. Phys. Chem. C.* **119**, 23638–23647 (2015).
48. Reshchikov M. A., Morkoç H. Luminescence properties of defects in GaN. *J. Appl. Phys.* **97**, (2005).
49. Levine, I. et al. Revisiting sub-band gap emission mechanism in 2D halide perovskites: the role of defect states. *J. Am. Chem. Soc.* **146**, 23437–23448 (2024).
50. Luo, J. et al. Efficient and stable emission of warm-white light from lead-free halide double perovskites. *Nature* **563**, 541–545 (2018).
51. Xing, Z. et al. Barrierless exciton self-trapping and emission mechanism in low-dimensional copper halides. *Adv. Funct. Mater.* **32**, 2207638 (2022).

52. Zhang, Y. et al. Self-trapped excitons in 2D SnP2S6 crystal with intrinsic structural distortion. *Adv. Funct. Mater.* **32**, 2205757 (2022).
53. Wu, B. et al. Uncovering the mechanisms of efficient upconversion in two-dimensional perovskites with anti-Stokes shift up to 220 meV. *Sci. Adv.* **9**, eadi9347 (2023).
54. Ni, L. et al. Real-time observation of exciton–phonon coupling dynamics in self-assembled hybrid perovskite quantum Wells. *ACS Nano* **11**, 10834–10843 (2017).
55. Straus, D. B. et al. Longer cations increase energetic disorder in excitonic 2D hybrid perovskites. *J. Phys. Chem. Lett.* **10**, 1198–1205 (2019).
56. Esmaielpour, H. et al. Role of exciton binding energy on LO phonon broadening and polaron formation in (BA)2PbI4 Ruddlesden–Popper Films. *J. Phys. Chem. C.* **124**, 9496–9505 (2020).
57. Fu, J. et al. Electronic states modulation by coherent optical phonons in 2D halide perovskites. *Adv. Mater.* **33**, 2006233 (2021).
58. Zhang, L. et al. Revealing the mechanism of pressure-induced emission in layered silver-bismuth double perovskites. *Angew. Chem. Int. Ed.* **62**, e202301573 (2023).
59. Han, J. et al. Pressure-induced free exciton emission in a quasi-zero-dimensional hybrid lead halide. *Angew. Chem. Int. Ed.* **63**, e202316348 (2024).
60. Wu, B. et al. Strong self-trapping by deformation potential limits photovoltaic performance in bismuth double perovskite. *Sci. Adv.* **7**, eabd3160 (2021).
61. Sui, X. et al. Zone-folded longitudinal acoustic phonons driving self-trapped state emission in colloidal CdSe nanoplatelet superlattices. *Nano Lett.* **21**, 4137–4144 (2021).
62. Thouin, F. et al. Phonon coherences reveal the polaronic character of excitons in two-dimensional lead halide perovskites. *Nat. Mater.* **18**, 349–356 (2019).
63. Quan, L. N. et al. Vibrational relaxation dynamics in layered perovskite quantum wells. *Proc. Natl. Acad. Sci.* **118**, e2104425118 (2021).
64. Debnath, T. et al. Coherent vibrational dynamics reveals lattice anharmonicity in organic–inorganic halide perovskite nanocrystals. *Nat. Commun.* **12**, 2629 (2021).
65. Fu, J., Ramesh, S., Melvin Lim, J. W. & Sum, T. C. Carriers, quasiparticles, and collective excitations in halide perovskites. *Chem. Rev.* **123**, 8154–8231 (2023).
66. Gong, X. et al. Electron–phonon interaction in efficient perovskite blue emitters. *Nat. Mater.* **17**, 550–556 (2018).
67. Jiang, X. et al. Broadband emission originating from the stereochemical expression of 6s2 lone pairs in two-dimensional lead bromide perovskites. *Dalton Trans.* **52**, 15489–15495 (2023).
68. Rojas-Gatjens, E., Silva-Acuña, C. & Kandada, A. R. S. Peculiar anharmonicity of Ruddlesden Popper metal halides: temperature-dependent phonon dephasing. *Mater. Horiz.* **9**, 492–499 (2022).
69. Yazdani, N. et al. Coupling to octahedral tilts in halide perovskite nanocrystals induces phonon-mediated attractive interactions between excitons. *Nat. Phys.* **20**, 47–53 (2024).
70. Eperon, G. E. et al. Formamidinium lead trihalide: a broadly tunable perovskite for efficient planar heterojunction solar cells. *Energy Environ. Sci.* **7**, 982–988 (2014).
71. Hase, M., Mizoguchi, K., Harima, H., Nakashima, S. -i & Sakai, K. Dynamics of coherent phonons in bismuth generated by ultrashort laser pulses. *Phys. Rev. B* **58**, 5448–5452 (1998).
72. Sun, L. et al. Phonon dephasing dynamics in MoS2. *Nano Lett.* **21**, 1434–1439 (2021).
73. Vallée, F. & Bogani, F. Coherent time-resolved investigation of LO-phonon dynamics in GaAs. *Phys. Rev. B* **43**, 12049–12052 (1991).
74. Buizza, L. R. V. & Herz, L. M. Polarons and charge localization in metal-halide semiconductors for photovoltaic and light-emitting devices. *Adv. Mater.* **33**, 2007057 (2021).
75. Wang, F. et al. Phonon signatures for polaron formation in an anharmonic semiconductor. *Proc. Natl. Acad. Sci.* **119**, e2122436119 (2022).
76. Leguy, A. M. A. et al. Dynamic disorder, phonon lifetimes, and the assignment of modes to the vibrational spectra of methylammonium lead halide perovskites. *Phys. Chem. Chem. Phys.* **18**, 27051–27066 (2016).
77. Cortecchia, D., Yin, J., Petrozza, A. & Soci, C. White light emission in low-dimensional perovskites. *J. Mater. Chem. C.* **7**, 4956–4969 (2019).

Acknowledgements

The authors greatly acknowledge the financial support from the National Key Research and Development Program (2023YFA1507002 and 2023YFA1407004), the Strategic Priority Research Program of the Chinese Academy of Sciences (XDB0770000), the Hundred Talents Program of Chinese Academy of Sciences (E4N851R1ZX), the National Science Foundation for Distinguished Young Scholars of China (22325301), the National Science Foundation for Excellent Young Scholars of China (62422512), the National Natural Science Foundation of China (22173025, 22073022, 62175061, 52172140, 52221001, 22503006, 22573023), J.Y. acknowledges financial support from Hong Kong Polytechnic University (P0053682 and P0055295), Research Grants Council of the Hong Kong Special Administrative (SAR) Region, China (Project No. PolyU 25300823 and PolyU 15300724). J.X. acknowledges financial support from Taishan Scholars Program, Qingdao Natural Science Foundation (25-1-1-168-zyyd-jch).

Author contributions

X.L. led the project. X.L., J.F., Y.Zhang, and C.Y. conceived the idea. X. L., B.W., and Y.Z. designed experiments. Y.Zhong and Z.Z. performed physical characterization. Y.Zhang, W.D., Y.T., and Y.Zhong conducted the temperature-dependent photoluminescence experiments. Y.Zhang, S.Y., Y. Gong, and X.B. conducted the TA experiments. J.X. and D.L. grew the samples. Y.Zhang, Y. Guo, M.F., C.Y., Y.X., and J.F. led the experimental analysis. Y.Zhang and X.B. measured the Raman spectra. J.Y. and S.L. performed the first principles DFT calculations. Y.Zhang, Y.Guo, M.F., J.F., and X.L. prepared the manuscript. All authors discussed the results and revised the manuscript. Y.Zhang, Y. Guo, M.F., and S.L. contributed equally to this work.

Competing interests

The authors declare no competing interests.

Additional information

Supplementary information The online version contains supplementary material available at https://doi.org/10.1038/s41467-026-68545-7.

Correspondence and requests for materials should be addressed to Jun Xing, Jun Yin, Jianhui Fu or Xinfeng Liu.

Peer review information *Nature Communications* thanks Song Jin and the other anonymous reviewer(s) for their contribution to the peer review of this work. A peer review file is available.